

Sparse Array Design for Near-Field MU-MIMO: Reconfigurable Array Thinning Approach

Ahmed Hussain, Asmaa Abdallah, *Member, IEEE*, Abdulkadir Celik, *Senior Member, IEEE*, Emil Björnson, *Fellow, IEEE* and Ahmed M. Eltawil, *Senior Member, IEEE*

Abstract—Future wireless networks, deploying thousands of antenna elements, may operate in the radiative near-field (NF), enabling spatial multiplexing across both angle and range domains. Sparse arrays have the potential to achieve comparable performance with fewer antenna elements. However, fixed sparse array designs are generally suboptimal under dynamic user distributions, while movable antenna architectures rely on mechanically reconfigurable elements, introducing latency and increased hardware complexity. To address these limitations, we propose a reconfigurable array thinning approach that selectively activates a subset of antennas to form a flexible sparse array design without physical repositioning. We first analyze grating lobes for uniform sparse arrays in the angle and range domains, showing their absence along the range dimension. Based on the analysis, we develop two particle swarm optimization-based strategies: a grating-lobe-based thinned array (GTA) for grating-lobe suppression and a sum-rate-based thinned array (STA) for multiuser sum-rate maximization. Simulation results demonstrate that GTA outperforms conventional uniform sparse arrays, while STA achieves performance comparable to movable antennas, thereby offering a practical and efficient array deployment strategy without the associated mechanical complexity.

Index Terms—Near-field, sparse arrays, array thinning, particle swarm optimization, MU-MIMO.

I. INTRODUCTION

FUTURE wireless networks are expected to deploy increasingly large antenna arrays, thereby extending communication into the radiating near-field (NF) regime [1]. Unlike the far-field (FF), where user equipments (UEs) are multiplexed solely in the angular domain, spherical wave propagation in the NF enables finite-depth beamforming that resolves UEs jointly in angle and range. This additional spatial dimension substantially enhances spatial multiplexing gains [2]. However, realizing large-aperture arrays with half-wavelength spacing may require thousands of antenna elements, leading to a significant increase in hardware cost, power consumption, and computational complexity.

Achieving high spatial multiplexing gain in multi-user multiple-input multiple-output (MIMO) systems necessitates strong orthogonality among the UE channel vectors to suppress inter-user interference. Sparse arrays offer a potential solution, especially in low-scattering environments, by leveraging larger

inter-element spacings to reduce spatial correlation and generate more diverse channels than half-wavelength arrays [3]. Nevertheless, uniform sparse arrays suffer from grating lobes, which cause strong interference by illuminating unintended directions. To address this limitation, non-uniform array geometries, such as coprime arrays [4] and array-position optimization techniques [5]–[7], have been investigated. More recently, movable antenna (MA) architectures have been proposed, wherein antenna elements can be physically reconfigured to match the instantaneous user distribution and enhance channel orthogonality [8], [9]. Despite their potential, MA-based designs rely on physically reconfigurable hardware and real-time repositioning, which introduce reliability concerns, latency overheads, and considerable system-level complexity. A key limitation of existing sparse array solutions is that they are either static, optimized for a specific user distribution and therefore suboptimal under different channel conditions, or mechanical, as in MA architectures that require continuous physical movement and high-precision hardware. Both approaches are thus challenging to implement in practical NF multi-user MIMO deployments.

To address these challenges, we propose a reconfigurable array thinning framework in which the full dense array remains physically fixed, but only a selected subset of antennas is activated to meet a desired performance objective. That is, rather than redesigning the array geometry or moving antennas, the system forms an effective sparse aperture by selectively switching elements on or off. Array thinning is a well-established technique in radar [10], where thinned arrays use fewer radiating elements than a fully populated aperture. Although only a subset of elements is used, the mainlobe beamwidth is preserved due to the unchanged aperture size, while the array gain is reduced proportionally with the number of active elements. The primary benefit is comparable spatial resolution to the full array and acceptable sidelobe levels, while enabling energy-efficient operation, reduced hardware complexity, and graceful degradation.

Accordingly, this paper extends the array-thinning concept to NF multi-user communication, enabling the design of dynamic, low-complexity sparse arrays. We address three fundamental research questions: First, although it is well known that exceeding half a wavelength yields grating lobes in the angular domain, it remains unclear whether similar phenomena also arise in the range domain. Second, we examine the achievable multiuser sum-rate when a thinned array is pre-optimized for grating-lobe suppression, and assess the performance gain compared to uniform sparse arrays. Third, we investigate how

Ahmed Hussain, Asmaa Abdallah, and Ahmed M. Eltawil are with Computer, Electrical, and Mathematical Sciences and Engineering (CEMSE) Division, King Abdullah University of Science and Technology (KAUST), Thuwal, 23955-6900, KSA. Abdulkadir Celik is with School of Electronics and Computer Science, University of Southampton, SO17 1BJ UK. Emil Björnson is with the School of Electrical Engineering and Computer Science, KTH Royal Institute of Technology, 100 44 Stockholm, Sweden. The work of E. Björnson was supported by the Grant 2022-04222 from the Swedish Research Council.

to design dynamic thinned arrays that maximize the multiuser sum-rate.

To address these questions, we first investigate grating lobes in the NF across both the angle and range domains. Grating lobes arise from the periodicity of the array factor, and understanding this phenomenon is critical for sparse array design. Building on the insights drawn from the analysis of grating lobes, we propose two types of sparse array designs using a particle swarm optimization (PSO)-based optimization framework. The first design, termed as grating-lobe-based thinned array (GTA), aims to suppress grating lobes in the NF. The second design, sum-rate-based thinned array (STA), is explicitly optimized to maximize the multiuser sum-rate. We benchmark the proposed designs against other sparse arrays, including sparse uniform linear array (SULA), pre-optimized thinned array (PTA), and moveable uniform linear array (MULA). Simulation results show that the STA outperforms other sparse arrays while achieving performance comparable to that of the MULA. The GTA matches the performance of the PTA, highlighting that grating-lobe-aware optimization effectively preserves aperture gain while suppressing interference arising due to grating lobes.

II. SYSTEM MODEL

We consider a base station (BS) equipped with a full uniform linear array (FULA) of N antennas with inter-element spacing $d = \frac{\lambda}{2}$, resulting in an aperture length $D = (N - 1)\frac{\lambda}{2}$. During operation, the BS activates only N_T antennas, forming a thinned array characterized by the thinning ratio $\text{TR} = \frac{N_T}{N}$. In a downlink free-space line-of-sight (LoS) scenario, the BS simultaneously serves K single-antenna UEs, where each data symbol s_k is precoded using the beamforming vector $\mathbf{w}_k \in \mathbb{C}^N$ and transmitted from the BS. The received signal at the k^{th} UE is expressed as

$$y_k = \mathbf{w}_k^H \mathbf{h}_k s_k + \sum_{j=1, j \neq k}^K \mathbf{w}_k^H \mathbf{h}_j s_j + z_k, \quad (1)$$

where z_k represents additive circularly symmetric complex Gaussian noise with variance σ^2 . The channel vector $\mathbf{h}_k \in \mathbb{C}^N$ between the BS and the k^{th} UE, is given by

$$\mathbf{h}_k = \sqrt{\beta_k} e^{-j \frac{2\pi}{\lambda} r_k} (\mathbf{b} \odot \mathbf{a}(\theta_k, r_k)), \quad \beta_k = \frac{\lambda^2}{(4\pi)^2 r_k^2}, \quad (2)$$

where \odot denotes the element-wise (Hadamard) product. The coefficient β_k captures the path loss, and $\mathbf{a}(\theta_k, r_k) \in \mathbb{C}^N$ is the NF array response vector corresponding to azimuth angle θ_k and range r_k . The vector $\mathbf{b} \in \{0, 1\}^N$ represents the binary thinning weights. An entry $b_n = 1$ indicates that the n^{th} antenna element is active, whereas $b_n = 0$ denotes a deactivated (thinned) element. In practice, this can be implemented using a dynamic sub-array architecture, in which an RF switch network allows each antenna element to be connected to any radio frequency (RF) chain, while inactive elements are terminated to ground. A more power-efficient alternative is a fixed sub-array-based architecture, where each RF chain is restricted to a predefined subset of antenna elements through a switch network. These architectures involve a fundamental trade-off between spectral efficiency and power efficiency. A detailed analysis of this trade-off is left for future work. The normalized

NF array response vector for the n^{th} antenna, is approximated as [11]

$$a_n(\theta, r) \approx \frac{1}{\sqrt{N}} e^{-j \frac{2\pi}{\lambda} \{nd \sin(\theta) - \frac{1}{2r} n^2 d^2 \cos^2(\theta)\}}, \quad (3)$$

which is valid when the UE range exceeds twice the aperture length, i.e., $r > 2D$. To suppress interference in (1), we employ a regularized zero-forcing precoder. The resulting achievable sum-rate is

$$\mathcal{R}_{\text{sum}} = \sum_{k=1}^K \log_2(1 + \Gamma_k), \quad (4)$$

where Γ_k denotes the signal-to-interference-plus-noise ratio of the k^{th} UE and is given by,

$$\Gamma_k = \frac{|\mathbf{w}_k^H \mathbf{h}_k|^2}{\sigma^2 + \sum_{j=1, j \neq k}^K |\mathbf{w}_j^H \mathbf{h}_k|^2}. \quad (5)$$

For a given UE distribution, the sum-rate in (4) can be optimized by adjusting antenna positions. However, real-time repositioning incurs high complexity, cost, and latency, as the optimization must be performed whenever the geometrical parameters of the channel change. To overcome this, we propose an array thinning strategy that activates only a subset of antennas to achieve performance comparable to the MULA. We formulate the antenna-activation task as an optimization over the activation vector $\mathbf{b} = [b_1, \dots, b_N]^T$. Let $f(\mathbf{b})$ denote a generic objective function (e.g., sum-rate). The antenna-selection problem is expressed as

$$\max_{\mathbf{b}} f(\mathbf{b}) \quad \text{s.t.} \quad \sum_{n=1}^N b_n = N_T, \quad (6)$$

The constraint $\sum_{n=1}^N b_n = N_T$ enforces the thinning ratio, ensuring that exactly N_T antennas remain active. While the overarching goal remains sum-rate maximization, we employ two alternative objective functions $f(\mathbf{b})$ which are detailed in Section IV.

III. GRATING LOBES IN THE NEAR-FIELD

Grating lobes introduce undesired interference that can significantly degrade the multiuser sum-rate. In this section, we analyze the SULA to investigate the occurrence of grating lobes in both the angular and range dimensions.

A. Grating Lobes in the Angle Domain

Consider an NF beam focused at the location (θ_0, r_0) . The corresponding beam pattern in the angle domain is obtained as

$$\begin{aligned} \mathcal{G}(\theta) &= |\mathbf{a}^H(\theta_0, r_0) \mathbf{a}(\theta, r)|^2 \\ &= \left| \frac{1}{N} \sum_{n=0}^{N-1} e^{j \frac{2\pi}{\lambda} n d (\sin \theta - \sin \theta_0)} e^{-j \frac{2\pi}{\lambda} \frac{n^2 d^2}{2} \left(\frac{\cos^2 \theta}{r} - \frac{\cos^2 \theta_0}{r_0} \right)} \right|^2 \\ &\stackrel{(a)}{\approx} \left| \frac{1}{N} \sum_{n=0}^{N-1} e^{j \frac{2\pi}{\lambda} n d (\sin \theta - \sin \theta_0)} \right|^2, \end{aligned} \quad (7)$$

where approximation (a) follows from the distance-ring condition $\frac{\cos^2(\theta)}{r} = \frac{\cos^2(\theta_0)}{r_0}$ [12]. This condition defines a set of range-angle pairs along which the beamwidth remains nearly constant. The simplified expression in (7) represents the array factor in the angle domain. We present Property 1 to review grating lobes in the angle domain and then use it to analyze grating lobes in the range domain.

Property 1 (Periodicity Condition of the Array Factor). Consider the discrete sequence $e^{j\phi_n(x)}$, where $x \in \{\theta, r\}$ and $\phi_n(x)$ denotes the phase contribution of the n^{th} antenna element. The sequence $e^{j\phi_n(x)}$ is periodic if and only if there exists a constant increment Δx such that [13]

$$\phi_n(x) - \phi_n(x_0) = 2\pi q, \quad q \in \mathbb{Z}, \quad (8)$$

where x_0 denotes the focused angle/range, and $x = x_0 + \Delta x$ is the observation angle/range at which the presence of a grating lobe is evaluated.

Applying (8) to the array factor expression in (7), the grating lobes occur when the phase shift between adjacent elements equals an integer multiple of 2π [13]

$$2\pi \frac{d}{\lambda} (\sin \theta - \sin \theta_0) = 2\pi q, \quad q \in \mathbb{Z}. \quad (9)$$

Solving for θ yields the following grating lobe condition:

$$\sin \theta_q = \sin \theta_0 + q \frac{\lambda}{d}, \quad q = \pm 1, \pm 2, \dots \quad (10)$$

Grating lobes appear at angles θ_q when the mainlobe is focused at $\theta_0 \in [-90^\circ, 90^\circ]$, provided that $|\sin \theta_q| = |\sin \theta_0 + q \frac{\lambda}{d}| \leq 1$. For a uniform linear array (ULA), the visible angular region is given by $\theta \in [-90^\circ, 90^\circ]$, so no grating lobes occur within this region when $d \leq \lambda/2$. In contrast, for $d > \lambda/2$, additional lobes appear at angular locations determined by (10). For example, when $d = 2\lambda$ and $\theta_0 = 0^\circ$, (10) reduces to $\sin \theta_q = \frac{q}{2}$, which satisfies $|\sin \theta_q| \leq 1$ for $q \in \{-1, 1\}$. The corresponding grating lobe angles are $\theta_q \in \{-30^\circ, 30^\circ\}$.

B. Absence of Grating Lobes in the Range Domain

The beam pattern in the range domain is obtained as the inner product of NF array response vectors given in (3), pointing to the same angle θ but different distances r and r_0 [11]

$$\mathcal{G}(\theta, r) = |\mathbf{a}^H(\theta, r_0) \mathbf{a}(\theta, r)|^2, \quad (11)$$

$$\stackrel{\text{(a)}}{=} \left| \frac{1}{N} \sum_{n=0}^{N-1} e^{-j \frac{2\pi}{\lambda} n^2 d^2 \cos^2(\theta) r_{\text{eff}}} \right|^2, \quad (12)$$

where $r_{\text{eff}} = \left| \frac{r-r_0}{2rr_0} \right|$ in (a). To assess the possibility of grating lobes in the range domain, the phase in (12) must satisfy the periodicity condition in (8):

$$\frac{2\pi}{\lambda} d^2 \cos^2(\theta) r_{\text{eff}} = 2\pi q, \quad q \in \mathbb{Z}, \quad (13)$$

Solving for r yields the following expression:

$$r_q = \frac{r_0 d^2 \cos^2(\theta)}{d^2 \cos^2(\theta) + 2qr_0 \lambda}. \quad (14)$$

However, unlike the angular domain, where the phase varies linearly with element index n , the phase in (12) varies quadratically. As a result, at the distances r_q given by (14), the individual element phases do not re-align coherently across the array, and the summation over n does not produce a secondary mainlobe; instead, only small ripples are formed. Furthermore, the resulting r_q values are either negative (for $q < 0$) or extremely small (for $q > 1$), rendering them physically impractical. Therefore, unlike the angular domain, grating lobes do not appear along the range dimension. To exemplify this with a numerical example, we consider a 256 element SULA with inter-element spacing $d = 2\lambda$ and an NF beam focused at $(\theta_0 = 0^\circ, r_0 = r_{\text{RD}}/30 = 346 \text{ m})$, where $r_{\text{RD}} = \frac{2D^2}{\lambda}$ denotes the Rayleigh distance. As shown in Fig. 1, we plot the resulting two-dimensional (2D) beam pattern along

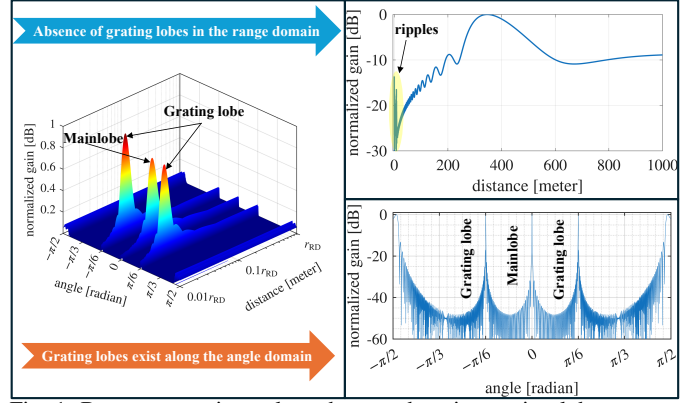


Fig. 1: Beam pattern in angle and range domain: grating lobes appear only in the angular domain. Here we set $f_c = 15 \text{ GHz}$, $N = 256$, $d = 2\lambda$, $r_0 = 346 \text{ m}$ and $r_{\text{RD}} = 10.3 \text{ km}$.

with the corresponding one-dimensional (1D) cuts in angle and range. In the 2D plot, two additional grating lobes emerge at $\theta = \pm \frac{\pi}{6}$, consistent with the angular positions predicted in the last subsection. In contrast, the range-domain response exhibits no grating lobes. This distinction is further clarified by the 1D angular and range patterns, which highlight the presence of grating lobes solely in the angular domain. Furthermore, small ripples are observed at short ranges in the 1D range-domain response. Specifically, the dominant ripple attains a level of -13 dB at a distance of 0.01 m .

IV. PROPOSED OPTIMIZATION METHODS

In this section, we explain the two proposed array-thinning strategies for optimizing the sum-rate in (4). The first method, GTA, suppresses grating lobes, while the second method, STA, directly maximizes the multiuser sum-rate.

A. PSO-based Array Thinning for Grating-Lobe Suppression

Grating lobes can be mitigated by disrupting the periodic structure of the SULA. Based on the results of Section III, we need to suppress grating lobes only in the angle domain. We consider the weighted angle-domain beam pattern of a ULA with N antennas, given by

$$\mathcal{G}(\mathbf{b}, \theta) = \left| \frac{1}{N} \sum_{n=0}^{N-1} b_n \odot e^{j \frac{2\pi}{\lambda} n d (\sin \theta - \sin \theta_0)} \right|^2, \quad (15)$$

The thinning problem aims to determine an optimal binary vector \mathbf{b} that minimizes the peak sidelobe level (PSLL) within a specified angular coverage region Θ_{cov} . Since the grating-lobe behavior varies with the angle θ_0 , the PSLL is defined as a function of θ_0 as

$$\text{PSLL}(\mathbf{b}, \theta_0) = 10 \log_{10} \left(\frac{\max_{\theta \in \mathcal{S}} \mathcal{G}(\mathbf{b}, \theta)}{\mathcal{G}(\mathbf{b}, \theta_0)} \right), \quad (16)$$

where \mathcal{S} denotes the sidelobe region excluding the mainlobe around θ_0 . As the steering angle θ_0 increases, additional grating lobes may appear. For a given antenna spacing d , more grating lobes appear as the angle is steered towards the endfire direction. Hence, we aim to design a thinning pattern that minimizes the PSLL over the maximum steering angle within the coverage interval Θ_{cov} . Accordingly, the optimization problem (6), where

$f(\mathbf{b}) = \text{PSLL}(\mathbf{b}, \theta_0)$, is formulated as

$$\min_{\mathbf{b}} \max_{\theta_0 \in \Theta_{\text{cov}}} \text{PSLL}(\mathbf{b}, \theta_0), \quad (17)$$

$$\text{s.t. } \text{PSLL}(\mathbf{b}, \theta_0) \leq \tau_{\text{PSLL}}, \quad (18)$$

$$\sum_{n=1}^N b_n = N_T, \quad (19)$$

$$b_n = 1, \quad n \in \mathcal{F}, \quad (20)$$

where τ_{PSLL} denotes the maximum allowable sidelobe level. The constraint in (19) enforces a fixed number of active antennas, while (20) ensures that a predefined set \mathcal{F} of mandatory active elements (e.g., the two edge elements) is always preserved to maintain the maximum aperture.

A direct binary optimization over the thinning vector is computationally intractable due to the combinatorial search space. To address this, we leverage PSO that optimizes the objective function by iteratively evaluating P candidate solutions. In PSO, each particle p represents a potential solution. More specifically, we adopt a PSO-based continuous relaxation, where each particle represents a continuous priority vector $\mathbf{x}^{(p)} \in [0, 1]^{N_v}$. Here, $N_v = N - |\mathcal{F}|$ denotes the number of variable (non-fixed) antenna positions. This vector is subsequently mapped to the binary thinning vector $\mathbf{b}^{(p)}$. The complete procedure is summarized in Algorithm 1. The initialization (lines 3–5) assigns each particle a random position $\mathbf{x}^{(p)}(0)$ and velocity $\mathbf{v}^{(p)}(0)$, constructs the corresponding binary vector $\mathbf{b}^{(p)}(0)$, and evaluates the initial cost $f^{(p)}(0) = f(\mathbf{b}^{(p)}(0)) = \text{PSLL}(\mathbf{b}^{(p)}(0), \theta_0)$. Each particle stores its personal best $\mathbf{P}_{\text{best}}^{(p)}$ and the globally best particle determines \mathbf{G}_{best} . At iteration t , the velocity of the particle p is updated (line 8) according to

$$\mathbf{v}^{(p)}(t+1) = \omega \mathbf{v}^{(p)}(t) + c_1 u_1 \left(\mathbf{P}_{\text{best}}^{(p)} - \mathbf{x}^{(p)}(t) \right) + c_2 u_2 \left(\mathbf{G}_{\text{best}} - \mathbf{x}^{(p)}(t) \right), \quad (21)$$

where ω is the inertia weight, c_1 and c_2 are acceleration coefficients, and $u_1, u_2 \sim \mathcal{U}(0, 1)$ are random scalars. The updated velocity yields a new position (line 9):

$$\mathbf{x}^{(p)}(t+1) = \mathbf{x}^{(p)}(t) + \mathbf{v}^{(p)}(t+1). \quad (22)$$

The entries of $\mathbf{x}^{(p)}(t+1)$ are clipped to the interval $[0, 1]$ (line 10). In line 11, a new thinning vector $\mathbf{b}^{(p)}(t+1)$ is constructed by activating the antenna indices corresponding to the $\text{Top}_{N_T - |\mathcal{F}|}$ entries of $\mathbf{x}^{(p)}(t+1)$ and appending the fixed set \mathcal{F} . The corresponding objective function $f^{(p)}(t+1)$ is evaluated using (16). Each particle updates its personal best $\mathbf{P}_{\text{best}}^{(p)}$ whenever $f^{(p)}(t+1)$ improves upon its previous value, and the global best \mathbf{G}_{best} is replaced whenever a particle attains the lowest cost across the swarm. This process repeats for n_{PSO} iterations, after which the optimal thinning vector \mathbf{b}_{opt} is obtained by mapping \mathbf{G}_{best} to its binary representation.

B. PSO-based Array Thinning for Sum-Rate Maximization

In this subsection, we explain the STA to maximize the achievable sum-rate in (4). We assume that range and angle information of the UEs is known at the BS. For K UEs with $\boldsymbol{\theta} = [\theta_1, \dots, \theta_K]$ and ranges $\mathbf{r} = [r_1, \dots, r_K]$, we construct the channel matrix $\mathbf{H} \in \mathbb{C}^{N \times K}$ based on (2). Similar to the structure of the grating-lobe problem, we enforce a fixed

Algorithm 1: PSO for Array Thinning

```

1 Input: Number of particles  $P$ , iterations  $n_{\text{PSO}}$ , variable indices  $N_v$ ,
   fixed set  $\mathcal{F}$ , active antennas  $N_T$ , PSO parameters  $(\omega, c_1, c_2)$ 
2 Output: Optimal thinning vector  $\mathbf{b}_{\text{opt}}$ 
3 Initialization:  $\mathbf{x}^{(p)}(0) \in [0, 1]^{N_v}$ ,  $\mathbf{v}^{(p)}(0) \in \mathbb{R}^{N_v}$ ,
4  $\mathbf{b}^{(p)}(0) = \text{Top}_{N_T - |\mathcal{F}|}(\mathbf{x}^{(p)}(0)) \cup \mathcal{F}$ ,  $f^{(p)}(0) = f(\mathbf{b}^{(p)}(0))$ ,
5  $\mathbf{P}_{\text{best}}^{(p)} = \mathbf{x}^{(p)}(0)$ ,  $\mathbf{G}_{\text{best}} = \mathbf{x}^{(p^*)}(0)$ ,  $p^* = \arg \min_p f^{(p)}(0)$ 
6 for  $t = 0$  to  $n_{\text{PSO}} - 1$  do
7   for  $p = 1$  to  $P$  do
8      $\mathbf{v}^{(p)}(t+1) \leftarrow$  // Refer Eq. (21)
9      $\mathbf{x}^{(p)}(t+1) \leftarrow$  // Refer Eq. (22)
10     $\mathbf{x}^{(p)}(t+1) \leftarrow \min(\max(\mathbf{x}^{(p)}(t+1), 0), 1)$ 
11     $\mathbf{b}^{(p)}(t+1) \leftarrow \text{Top}_{N_T - |\mathcal{F}|}(\mathbf{x}^{(p)}(t+1)) \cup \mathcal{F}$ 
12     $f^{(p)}(t+1) = f(\mathbf{b}^{(p)}(t+1))$  // Refer Eq. (16)
13    if  $f^{(p)}(t+1) < f(\mathbf{P}_{\text{best}}^{(p)})$  then
14       $\mathbf{P}_{\text{best}}^{(p)} \leftarrow \mathbf{x}^{(p)}(t+1)$ 
15    end
16    if  $f^{(p)}(t+1) < f(\mathbf{b}(\mathbf{G}_{\text{best}}))$  then
17       $\mathbf{G}_{\text{best}} \leftarrow \mathbf{x}^{(p)}(t+1)$ 
18    end
19  end
20 end
21  $\mathbf{b}_{\text{opt}} = \text{Top}_{N_T - |\mathcal{F}|}(\mathbf{G}_{\text{best}}) \cup \mathcal{F}$ 

```

number of active N_T antennas and a set \mathcal{F} of mandatory active indices. The optimization problem (6) is reformulated as sum-rate maximization problem, where $f(\mathbf{b}) = \mathcal{R}_{\text{sum}}(\mathbf{b})$, and is given by

$$\max_{\mathbf{b}} \mathcal{R}_{\text{sum}}(\mathbf{b}), \quad (23)$$

$$\text{s.t. } \sum_{n=1}^N b_n = N_T, \quad b_n = 1 \quad n \in \mathcal{F}. \quad (24)$$

The optimization problem in (23) is combinatorial and NP-hard. Therefore, we adopt the same continuous-relaxation PSO framework described in the previous subsection. Each particle p maintains a continuous priority vector $\mathbf{x}^{(p)} \in [0, 1]^{N_v}$, where $N_v = N - |\mathcal{F}|$ denotes the number of variable antenna positions. A binary thinning vector $\mathbf{b}^{(p)}$ is obtained by activating all fixed indices and selecting $(N_T - |\mathcal{F}|)$ entries with the largest values in $\mathbf{x}^{(p)}$. The main distinction from the grating-lobe suppression formulation lies in the objective: the cost function is now the sum-rate ($f(\mathbf{b}) = \mathcal{R}_{\text{sum}}(\mathbf{b})$), whereas all PSO update rules remain unchanged. In particular, in line 10 of Algorithm 1, the cost is computed using the sum-rate expression in (4).

V. SIMULATION RESULTS

We evaluate the performance of the proposed GTA and STA designs by comparing them against several benchmark array configurations. In our setup, the BS employs a FULA with $N = 320$ antennas, while the thinned configurations activate only $N_T = 32$ antennas, yielding a thinning ratio of $\text{TR} = \frac{1}{10}$. The carrier frequency is 30 GHz and signal-to-noise ratio (SNR) is set to 20 dB. The following benchmark arrays are considered:

- **FULA:** A conventional ULA with $N = 320$ antennas and spacing $d = \frac{\lambda}{2}$, serving as an upper bound.
- **MULA:** A movable ULA with $N = 32$ antennas where antenna positions are optimized within $[-80\lambda, 80\lambda]$ using PSO for each channel realization.
- **PTA:** A thinned array with $N_T = 32$ active antennas

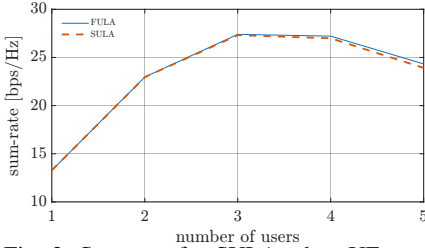


Fig. 2: Sum-rate for SULA when UEs are distributed only along the range.

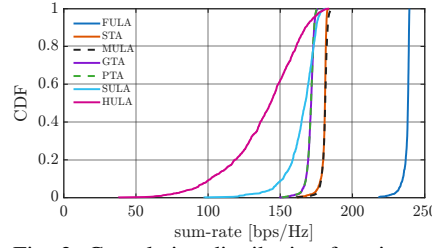


Fig. 3: Cumulative distribution function of the sum-rate across different sparse arrays.

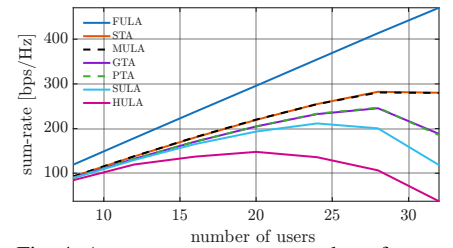


Fig. 4: Average sum-rate vs. number of users for different sparse arrays.

selected using statistical channel state information (CSI), following the approach presented in [3].

- **SULA:** A sparse ULA with $N_T = 32$ antennas and uniform spacing $d = 5\lambda$, chosen to match the aperture of the FULA.
- **Half-wavelength uniform linear array (HULA):** A compact ULA with $N_T = 32$ antennas and $d = \frac{\lambda}{2}$.

Except for the compact HULA, all configurations share the same aperture length to ensure a fair comparison. We keep the PSO parameters as given in [3].

We begin with a scenario where all UEs are aligned at the same boresight angle $\theta = 0^\circ$ and randomly distributed along the range axis, i.e., $r \sim \mathcal{U}[2D = 3.18 \text{ m}, \frac{r_{\text{RD}}}{7} = 72.6 \text{ m}]$, where $\frac{r_{\text{RD}}}{7}$ is the maximum beamfocusing distance at boresight [11]. Fig. 2 compares the sum-rate performance of the FULA and the SULA, with the beamforming gain normalized by the number of antenna elements. The two configurations exhibit nearly identical performance since (i) they share the same physical aperture and (ii) grating lobes do not occur along the range dimension for the SULA. Nevertheless, the SULA exhibits slightly elevated sidelobe levels relative to the FULA, which accounts for the marginal sum-rate degradation.

Next, we consider downlink transmission to $K = 16$ UEs, whose polar coordinates are generated according to $r \sim \mathcal{U}[2D = 3.18 \text{ m}, \frac{r_{\text{RD}}}{7} = 72.6 \text{ m}]$ and $\theta \sim \mathcal{U}[-\frac{\pi}{3}, \frac{\pi}{3}]$. Fig. 3 illustrates the cumulative distribution function (CDF) of the achievable sum-rate for all considered schemes. As expected, the FULA delivers the highest performance due to its full aperture and maximum beamforming gain. The proposed STA achieves performance comparable to that of the MULA. Moreover, it attains approximately 75% of the FULA sum-rate while utilizing only 10% of the active elements. The GTA attains performance comparable to the PTA, indicating that grating-lobe suppression effectively reduces interference and enhances sum-rate. Although GTA removes grating lobes, its sidelobes remain relatively elevated due to irregular element spacing and the reduced number of active antennas. The sum-rate of GTA is on average 5% lower than that of the STA. However, the GTA is pre-optimized, whereas the STA requires more frequent updates depending on the channel geometrical parameters.

Finally, Fig. 4 shows the average sum-rate versus the number of served UEs. The proposed STA consistently outperforms all sparse baselines. For moderate system loading, i.e., when $\frac{N_T}{K} > 1$, the sum-rate increases approximately linearly and gradually saturates as $\frac{N_T}{K}$ approaches unity, due to the transition to an interference-limited regime. Furthermore, the

proposed STA achieves sum-rate performance comparable to the MULA. Importantly, array thinning provides a hardware-efficient solution that reduces implementation complexity and power consumption without requiring mechanical repositioning of antenna elements. Moreover, it enables graceful performance degradation, since faulty elements can be deactivated and the thinned array configuration can be dynamically re-optimized.

VI. CONCLUSION

This work introduced a dynamic array thinning framework to optimize multi-user sum-rate in the near field. The proposed STA achieves performance comparable to the MULA while avoiding the hardware challenges associated with MULA. Future work will explore replacing the PSO with a deep learning-based solution to mitigate the computational complexity of the current optimization approach.

REFERENCES

- [1] A. Hussain, A. Abdallah, A. Celik, and A. M. Eltawil, "Near-field ISAC: Synergy of dual-purpose codebooks and space-time adaptive processing," *IEEE Wireless Commun.*, vol. 32, no. 4, pp. 64–70, 2025.
- [2] A. Abdallah, A. Hussain, A. Celik, and A. M. Eltawil, "Exploring frontiers of polar-domain codebooks for near-field channel estimation and beam training: A comprehensive analysis, case studies, and implications for 6G," *IEEE Signal Process. Mag.*, vol. 42, no. 1, pp. 45–59, 2025.
- [3] A. Irshad, A. Kosasih, V. Petrov, and E. Björnson, "Pre-optimized irregular arrays versus movable antennas in multi-user MIMO systems," *IEEE Wireless Commun. Lett.*, vol. 14, no. 8, pp. 2656–2660, 2025.
- [4] C. Zhou, C. You, H. Zhang, L. Chen, and S. Shi, "Sparse array enabled near-field communications: Beam pattern analysis and hybrid beamforming design," *arXiv preprint arXiv:2401.05690*, 2024.
- [5] K. Chen, C. Qi, G. Y. Li, and O. A. Dobre, "Near-field multiuser communications based on sparse arrays," *IEEE J. Sel. Topics Signal Process.*, vol. 18, no. 4, pp. 619–632, 2024.
- [6] Z. Wang, H. Xu, G. Zhang, X. Huang, and X. He, "Sparse-array-enabled wideband beamforming for near-field multiuser communications," *IEEE Internet Things J.*, vol. 12, no. 22, pp. 48 428–48 440, 2025.
- [7] E. Björnson, A. Irshad, Ö. T. Demir, G. T. F. de Abreu, A. Kosasih, and V. Petrov, "From antenna abundance to antenna intelligence in 6G gigantic MIMO systems," *arXiv preprint arXiv:2601.08326*, 2026.
- [8] L. Zhu, W. Ma, and R. Zhang, "Movable antennas for wireless communication: Opportunities and challenges," *IEEE Commun. Mag.*, vol. 62, no. 6, pp. 114–120, 2024.
- [9] L. Zhu, W. Ma, W. Mei, Y. Zeng, Q. Wu, B. Ning, Z. Xiao, X. Shao, J. Zhang, and R. Zhang, "A tutorial on movable antennas for wireless networks," *IEEE Commun. Surv. Tutor.*, 2025.
- [10] R. Haupt, "Thinned arrays using genetic algorithms," *IEEE Trans. Antennas Propag.*, vol. 42, no. 7, pp. 993–999, 1994.
- [11] A. Hussain, A. Abdallah, and A. M. Eltawil, "Redefining polar boundaries for near-field channel estimation for ultra-massive MIMO antenna array," *IEEE Trans. Wireless Commun.*, vol. 24, no. 10, pp. 8193–8207, 2025.
- [12] H. Zhang, C. You, and C. Zhou, "Near-field beam-focusing pattern under discrete phase shifters," *IEEE Trans. Wireless Commun.*, pp. 1–1, 2025.
- [13] R. C. Hansen, *Phased array antennas*. John Wiley & Sons, 2009.